

Characterizing shallow fault zones by integrating profile, borehole and array measurements of seismic data and distributed acoustic sensing

Nikolaus Rein^{1,2}  | Marius P. Isken³ | Dorina Domigall^{2,4} | Matthias Ohrnberger² |
Katrin Hannemann^{1,5}  | Frank Krüger² | Michael Korn¹ | Torsten Dahm^{2,3}

¹Institute of Geophysics and Geology, Leipzig University, Leipzig, Germany

²Institute of Geosciences, University of Potsdam, Potsdam-Golm, Germany

³German Research Centre for Geosciences, Physics of Earthquakes and Volcanoes, Potsdam, Germany

⁴Tauber Geo-Consult Geowissenschaftler & Ingenieure GmbH, Greven, Germany

⁵Institute of Geophysics, University of Münster, Münster, Germany

Correspondence Nikolaus Rein, Institute of Geosciences, University of Potsdam, Institute of Geosciences, Potsdam-Golm, 14476, Germany.
Email: lerbs@uni-potsdam.de

Funding information

Deutsche Forschungsgemeinschaft; Saxon State Office for Environment, Agriculture and Geology,

Abstract

Within the framework of the Intercontinental Scientific Drilling Programme (ICDP) ‘Drilling the Eger Rift’ project, five boreholes were drilled in the Vogtland (Germany) and West Bohemia (Czech Republic) regions. Three of them will be used to install high-frequency three-dimensional (3D) seismic arrays. The pilot 3D array is located 1.5 km south of Landwüst (Vogtland). The borehole, with a depth of 402 m, was equipped with eight geophones and a fibre optic cable behind the casing used for distributed acoustic sensing (DAS) measurements. The borehole is surrounded by a surface array consisting of 12 seismic stations with an aperture of 400 m. During drilling, a highly fractured zone was detected between 90 m and 165 m depth and interpreted as a possible fault zone. To characterize the fault zone, two vertical seismic profiling (VSP) experiments with drop weight sources at the surface were conducted. The aim of the VSP experiments was to estimate a local 3D seismic velocity tomography including the imaging of the steep fault zone. Our 3D tomography indicates P-wave velocities between 1500 m/s and 3000 m/s at shallow depths (0–20 m) and higher P-wave velocities of up to 5000 m/s at greater depths. In addition, the results suggest a NW–SE striking low-velocity zone (LVZ; characterized by $V_p = 1500\text{--}3000$ m/s), which crosses the borehole at a depth of about 90–165 m. This LVZ is inferred to be a shallow non-tectonic, steep fault zone with a dip angle of about 60°. The depth and width of the fault zone are supported by logging data as electrical conductivity, core recovery and changes in lithology. In this study, we present an example to test and verify 3D tomography and imaging approaches of shallow non-tectonic fault zones based on active seismic experiments using simple surface drop weights as sources and borehole chains as well as borehole DAS behind casing as sensors, complemented by seismic stand-alone surface arrays.

KEYWORDS

borehole, seismic array, tomography, travelttime

This is an open access article under the terms of the [Creative Commons Attribution-NonCommercial-NoDerivs](https://creativecommons.org/licenses/by-nc-nd/4.0/) License, which permits use and distribution in any medium, provided the original work is properly cited, the use is non-commercial and no modifications or adaptations are made.

© 2024 The Authors. *Near Surface Geophysics* published by John Wiley & Sons Ltd on behalf of European Association of Geoscientists and Engineers.

INTRODUCTION

Tomographic imaging of steep, shallow fault zones is an essential part of geothermal studies (Chen & Huang, 2015). Permeable fault zones are suitable as reservoir targets as they are pathways for high-temperature fluid flows (e.g., Corbel et al., 2012; Chen & Huang, 2015; Goyal & Kassoy, 1980). Earthquakes can also occur at fault zones when the stress field changes during exploration or production of a geothermal field. Thus, knowing a fault's location and hydrothermal potential as well as the fault zone's hazard is crucial for geothermal studies before drilling a deep borehole.

Geothermal studies previously detected non-tectonic fault zones using various types of seismic methods and approaches, such as first arrivals (e.g., Lutter et al., 1999), diffractions (e.g., Demanet et al., 2001), ground-penetrating radar (GPR; e.g., Cai et al., 1996), surface wave inversions (e.g., Ivanov et al., 2006) and shallow reflection imaging (e.g., Improtá & Bruno, 2007; Miller et al., 1989; Stephenson et al., 1993). These methods remain challenging, that is, in terms of penetration depth. GPR allows high-resolution imaging but is often limited to a depth of a few metres (Demanet et al., 2001). Imaging the subsurface on a fault-width scale with high-frequency surface waves (e.g., multichannel analysis of surface waves) is limited to a depth of tens of metres. The detection of fault zones using seismic reflections is challenging because high-quality reflections are often disturbed by near-surface effects (e.g., scattering, wave multiples, ground-rolls) and are also limited to the depth of investigation (Improtá & Bruno, 2007). In this study, we present an example to test and verify three-dimensional (3D) tomography and imaging approaches of shallow non-tectonic fault zones based on active seismic experiments using drop weights as sources and a 3D seismic array consisting of continuously recording stand-alone surface stations and vertical borehole geophones and fibre optic cables, which can be a low-cost alternative in a seismic exploration of geothermal sites.

Our study area (Figure 1) is located in West Bohemia (Czech Republic) and the Vogtland region (Germany), which are well known for their high seismicity (e.g., earthquake swarms), magmatic underplating with mantle-derived fluid flows and the degassing of mantle CO₂ at the surface (e.g., Dahm et al., 2013). The persistent occurrence of earthquake swarms has been known since the Middle Ages, and some swarms were studied in detail before instrumental seismology (e.g., Credner, 1898). Since 1984, the swarm activity is highest near the small village Nový Kostel in the Czech Republic (Figure 1a) and includes earthquakes with magnitudes up to M_L 4.5 and focal depths mainly in the upper crust between 6–15 km (e.g., Horálek & Fischer, 2010). Although it is generally accepted that fluid processes ultimately trigger the earthquake swarms in the region (e.g., Hainzl & Fischer, 2002; Bräuer et al.,

2003; Hainzl et al., 2012), it is still unclear how much of the seismic activity is controlled by tectonic (e.g., Vavryčuk, 2011; Vavryčuk et al., 2013), magmatic (e.g., Dahm et al., 2013; Horálek & Fischer, 2008; Hrubcová et al., 2013) or volcanic processes (Dahm et al., 2000, 2008).

Funded by the International Continental Scientific Drilling Program (ICDP, project *Drilling the Eger Rift*), five shallow boreholes were drilled between 2019 and 2022 (Figure 1a) and are instrumented for continuous monitoring of earthquake swarms and fluid flows (Dahm et al., 2013; Fischer et al., 2022). The 402-m deep drill site S1 in the Saxonian Vogtland (Germany) is located in the Western Ore Mountains at the northern edge of the Cheb Basin (Figure 1a,b), and monitoring is realized with a three-dimensional (3D) high-frequency three-component (3C) seismic array. Inside the water-filled borehole, eight 3C borehole geophones with eigenfrequencies of 10 Hz were installed in 2020 (Figure 1c). A seismic surface array consisting of 12 seismic 3C 4.5-Hz geophones with an aperture of 400 m was additionally built on the surface around the wellhead (Figure 1b). Behind the casing, a tight-buffer fibre optic cable for distributed acoustic sensing (DAS) measurements is cemented. DAS measures the strain rate along the fibre optic cable. Technically, an interrogator sends coherent laser pulses through a fibre optic cable. The coherent light pulse of the laser is recorded against time and thus can be used to calculate the phase and the amplitudes of the recorded signals. The output signal is the amplitude of the strain rate. The measurement principle of DAS is described in, for example, Othonos (2000) and Lellouch et al. (2019). Due to the high vertical resolution of the fibre optic cable, the signals improve the resolution in the well and thus minimize the uncertainties with depth (Nizkous et al., 2015).

During the drilling of S1, a steep fault zone crossing the borehole at depths of 90–165 m was detected and first recognized by an unusually high loss of drill mud. The fault zone was later confirmed in the geological characterization of the drill cores (Fischer et al., 2022; Hergesell, 2022). After its recognition in the well, the surface trace of the fault could be inferred from a combined analysis of surface morphology and existing geological-tectonic maps (Saxon State Office for Environment, Agriculture and Geology, 2022). The fault outcrops at a distance of about 90 m from the well and strikes in an NW-SE direction, indicating a dip angle of about 60°.

In order to image the fault zone, two vertical seismic profiling (VSP) experiments were conducted, using (1) a portable energy source (seismic impulse source system), (2) a weight drop, and (3) a seismic vibrator source to actively generate seismic waves at different locations and variable borehole offsets at the surface. The principle of VSP is explained in, for example, Balch and Lee (1984). The main objective of the VSP

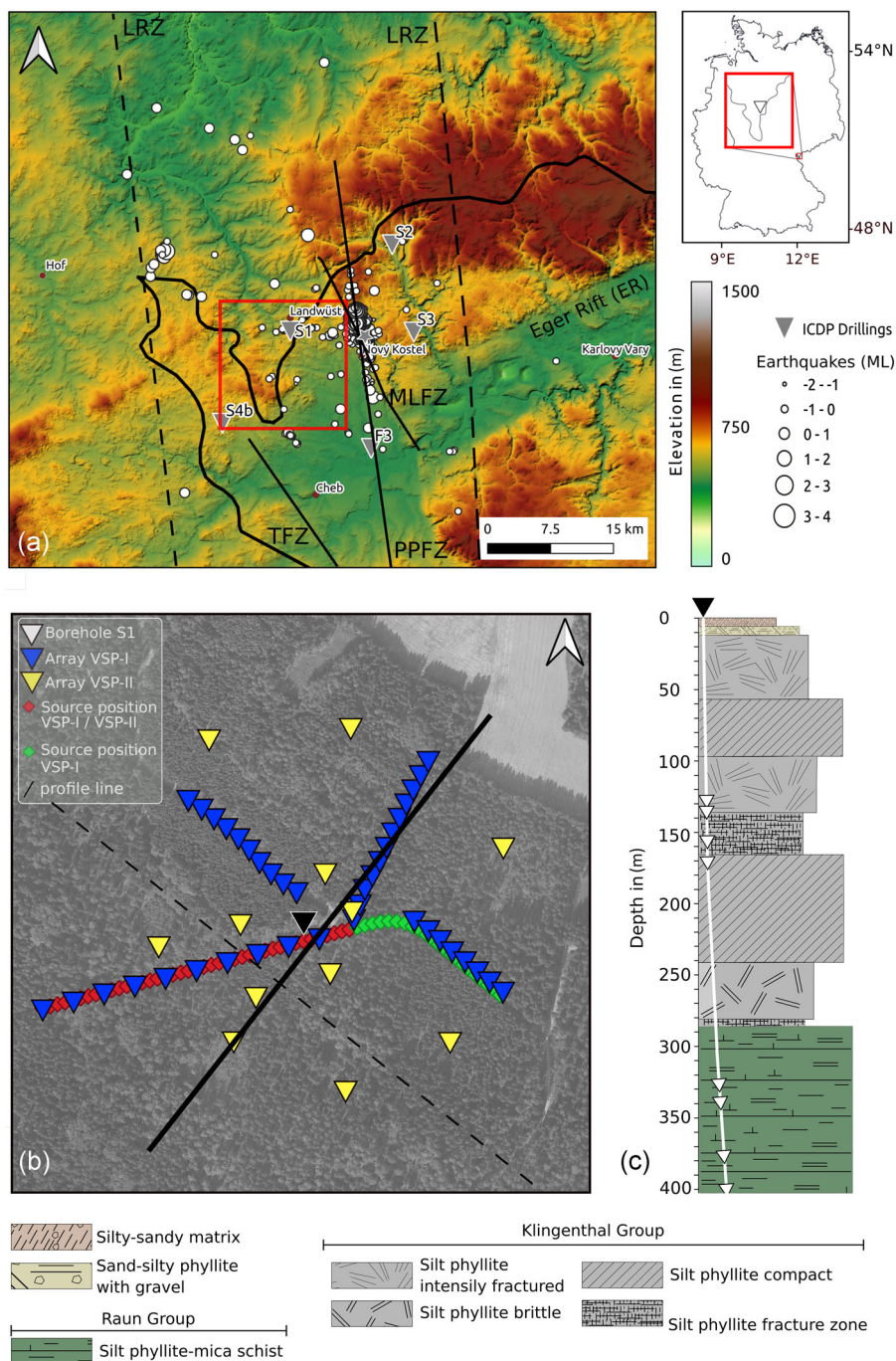


Figure 1 (a) Overview map showing the ICDP Drilling Site in West Bohemia and Vogtland (grey triangles). S1 (red box) is located close to the border of the Czech Republic in the Saxonian Vogtland. The black lines show the fault zones in the region after Fischer et al. (2014): Mariánské Lázně fault zone (MLFZ), Tachov fault zone (TFZ) and Počátky Plesná fault zone (PPFZ). The Nový Kostel focal zone is presented by a grey star. The black dashed lines show the area of the Leipzig Regensburg fault zone (LRZ). The white dots show the distribution of the earthquakes in the region of Vogtland/W-Bohemia from December 2020 to April 2021. (b) Seismic array configuration and source positions. The position of the well is presented by the back-edged white triangle. The blue triangles (40 sensors) show the distribution of the temporary seismic surface array for the first VSP experiment. The yellow triangles (12 sensors) represent the permanent surface array of S1 used for the second VSP experiment. The red and green diamonds show the source positions for both VSP experiments and only the red diamonds show the source positions used for the second VSP experiment. The black dashed line shows the fault zone crossing the study area in the NW-SE direction after Saxon State Office for Environment, Agriculture and Geology (2022) and the black line is the SW-NE profile normal to the fault zone corresponding to the vertical section of Figure 7. Map data are from Bing Aerial (© Microsoft). (c) Sketch of the borehole showing the borehole sensor (black-edged white triangles) distribution with depth and the lithology obtained by the drill core (modified after Fischer et al., 2022).

experiments was to generate a comprehensive dataset to perform a local 3D seismic velocity tomography to characterize the uppermost 400 m of the site including the steeply crossing fault zone. Seismic imaging and characterization of steep faults remain challenging, and the available multi-sensor, multi-source dataset is outstanding for testing tomographic and imaging approaches for fault zone characterization. The experiment also identified difficulties and sources of error in the integration of seismic surface and borehole data with DAS datasets that may be relevant to other applications.

We first describe the geological setting and site instrumentation, then the data integration and processing and finally the 3D tomography results are presented and discussed.

STRUCTURAL AND GEOLOGICAL SETTING

Lithology and well logging

The West Bohemia and Vogtland region is located in the NW part of the Bohemian Massif and is situated among three structural units of the Variscan age: the Saxothuringian, the Teplá-Barrandian and the Moldanubian (Babuška et al., 2007). These units are intersected at a small-scale basin (Cheb basin) by the ENE-WSW striking Cenozoic Eger Rift (Bräuer et al., 2009) and the N-S striking seismically active Leipzig Regensburg Fault Zone with a length of about 700 km and a width of about 40 km (e.g., Bankwitz et al., 2003) shown in Figure 1a. In addition, the region contains faults with different orientations, most prominent are the NNW-SSE striking Mariánské Lázně Fault Zone and the almost N-S trending Počátky-Plesná Fault Zone (Bankwitz et al., 2003; Hrubcová et al., 2017), which both intersect at the NNW-SSE striking Nový Kostel focal zone (see, Figure 1a) where more than 80% of the regional seismic energy has been released within the last decades (Fischer & Michálek, 2008). In addition, the NW-SE striking Tachov Fault Zone, shown in Figure 1a, is located at the western edge of the Cheb Basin with four Quaternary volcanoes (Hrubcová et al., 2017).

The lithology of the region is dominated by metamorphic rocks such as quartzite and different types of phyllite of Ordovician and Cambrian age (Saxon State Office for Environment, Agriculture and Geology, 2022). Quartzites are non-foliated metamorphic sandstones. Phyllites are foliated metamorphic rocks. Their metamorphic grade is low to middle, between slate and mica schist (Haldar, 2020). The mineral composition of phyllites is quartz, mica (mainly muscovite) and chlorite which lead to an anisotropic behaviour. Its crystal structure varies with direction. Therefore, a variation of

P-wave velocities with direction might be expected for this medium (Özbek et al., 2018).

The study area with the 402-m borehole S1 is located in the Western Ore Mountains in the Vogtland region (Germany) at the northern edge of the Cheb Basin (cf. Figure 1a). A NW-SE striking fault zone crosses the study area (cf., Figure 1b, black dashed line), which has been listed as an uncertain fault zone (Saxon State Office for Environment, Agriculture and Geology, 2022). As we show below, the fault zone crosses the borehole at a depth of 90–165 m, which was first recognized by an increased loss of mud during the drilling. Figure 2 shows the logging data of the core recovery and the electrical conductivity (EC) with depth (for more information, see Fischer et al., 2022). The red lines mark the depths between 90 m and 165 m. The core recovery is the amount of rock recovered as a core during drilling and gives an indication of the quality of the rock. For example, a high core recovery is given when the rock is solid and unbroken. Consequently, a poor core recovery is an indication that the material is fractured or weathered which is usually associated with loss of cores additional to drill mud. Figure 2a shows a poor core recovery close to the surface in depths smaller than 50 m. However, there is also a poor recovery in greater depths between 90–165 m and 360–390 m. A high EC is expected in saturated, permeable fault zones. At a depth of 0–90 m, the EC is between 0–0.0019 mS/m with a median of 0.0016 mS/m. At a depth of 90–165 m, the EC increases to a maximum of 0.0182 mS/m (median: 0.0075 mS/m). At greater depths, the EC decreases again and the median EC is 0.0020 mS/m (Figure 2b).

Figure 1c shows a sketch of the local lithology based on the drill core. The lithology at the well consists of a layer of soil and weathered material (mainly a silty-sandy matrix and sand-silty phyllites with gravels) up to 12.5 m depth. At a depth of 12.5–285 m, the lithology changes to a silt phyllite of the Klingenthal Group with different stages of fracturing. More precisely, the silt phyllite within the Klingenthal Group is intensely fractured at depths of 95–135 m and at a depth of 135–165 m is a fracture zone (Figure 1c). At a depth of 285 m, the lithology changes to a silt phyllite-mica schist of the Raun Group up to the bottom of the borehole at a depth of 402 m (Fischer et al., 2022).

VSP experiments

We conducted two VSP experiments in January (VSP-I) and November 2020 (VSP-II) using a suite of different active sources and a 3D–3C seismic array (see, Table 1). Surface geophones recorded as stand-alone stations continuously at a sampling rate of 400 Hz on DATA-CUBE³ loggers for both VSP experiments. For VSP-I, we installed 4.5 Hz geophones along linear pro-

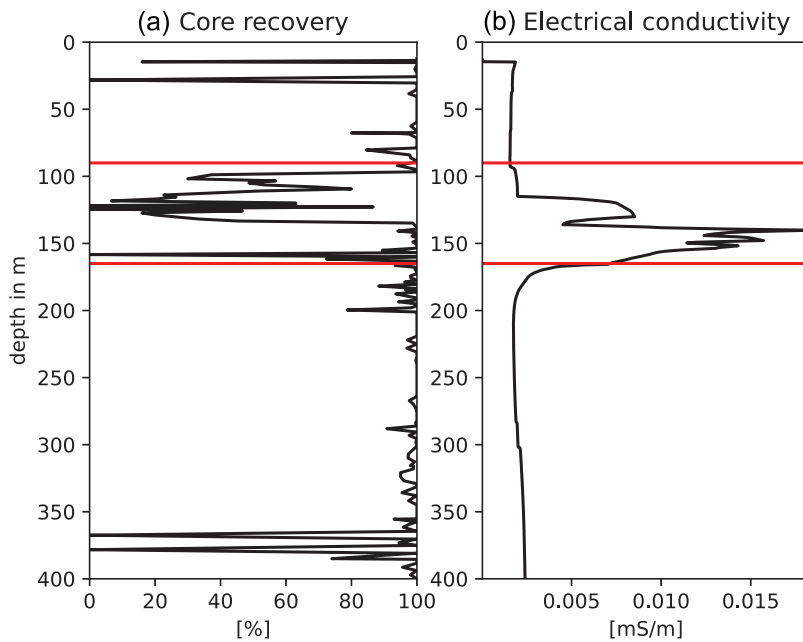


Figure 2 (a) Core recovery in per cent and (b) electrical conductivity in mS/m measured with depths obtained by the bore logging measurements. The red horizontal lines show the approximate depth (90–165 m) of the fault zone crossing the borehole. There is a "(" missing in Fig. 2b

Table 1 Details of the seismic instrumentation for both VSP experiments. f_s shows the sampling rate in hertz, and f_e is the eigenfrequency in hertz of the seismic sensors. The distribution of the sensors for both experiments is shown in Figure 1a (surface array) and c (vertical array). The DAS cable was only used during the second VSP experiment.

Surface array	Sensors	f_e (Hz)	f_s (Hz)	Aperture (m)
VSP-I	40	4.5	400	600 × 300
VSP-II	12	4.5	400	400 × 400
Borehole	Sensors	f_e (Hz)	f_s (Hz)	
VSP-I	8	10	400	
VSP-II	8	10	1000	
Silixa iDAS v.2	Gauge length	f_e	f_s	
VSP-II	10		1000	

files (four profiles between 200 m and 500 m in length), 40 in total and measured the geophone positions with a total station and a tape measure. Three linear profiles have a geophone spacing of 20 m, and the WSW-ENE-oriented profile has a geophone spacing of 40 m (see, Figure 1a, blue triangles). For VSP-II, the surface stations consisted of 12 distributed 4.5 Hz geophones with a total aperture of 400 m (see, Figure 1a, yellow triangles), which is also the final surface array installed at S1. A more detailed description of S1 can be found in Fischer et al. (2022). Eight 3C geophones with a corner frequency of 10 Hz were deployed in the borehole for the experiments. They were connected by DATA-CUBE³ (VSP-I) and Earth Data Logger (VSP-II). The sampling rate of the borehole chain was set to 400 Hz (VSP-I) and 1000 Hz (VSP-II), respectively. The coordinates of the borehole sensors were retrieved from the well logging measurements and the design of the linear

chain, where the sensors are distributed in two depth clusters. The first cluster contains four borehole sensors at depths between 120 m and 170 m. The second cluster consisting of four borehole sensors is located at depths between 320 m and 400 m (cf., Figure 1c). For VSP-II, we connected a Silixa iDAS v.2 interrogator to the fibre optic cable which is permanently cemented behind the casing to measure the axial strain rate along the cable at 1 m channel spacing with 1000 sps. For analysis, the data were downsampled to 250 Hz.

Different types of seismic sources were tested in VSP-I, comprising a Seismic Impulse Source System (SISSY), a seismic shear-wave vibrator source (ELVIS, ELectrodynamic VIbrator System) and a weight drop (SDD 6600). The data obtained by the ELVIS source has not been processed yet and is therefore not shown here. The weight drop has a weight of 340 kg and was released from a height of 2 m above the ground. The vertical impact of the weight dominantly induces P-waves. The weight drop had the strongest energy and was used in both VSP experiments. The weight drop, therefore, is the basis of the 3D tomographic analysis in this paper. A total of 86 shot points were realized with a spacing of 10 m (see, Figure 1a, green and red diamonds for VSP-I, red diamonds for VSP-II). The most distant shot point of the weight drop was 400 m from the well. We also released the weight drop at three positions with distances of 650–1000 m from the well. Due to the poor ray coverage of these single distant shots, we excluded them from the VSP tomography calculation. While single shots were used for VSP-I, we repeated the shots three times for VSP-II (red diamonds) in order to be able to stack the recordings and to enhance the signal-to-noise ratio (SNR), which was particularly useful for the DAS borehole measurements.

DATA ANALYSIS

Traveltimes

Since we used different seismic instruments, we removed the long-period trend and the instrument response in order to obtain the true amplitude information and thus to make the amplitudes comparable. The seismic amplitudes recorded by the geophones were restituted to ground velocity. The DAS amplitudes are shown as strain rate. Figure 3a shows the weight drop induced seismic signals measured at the borehole chain and one exemplary surface sensor. The corresponding frequency spectra are shown in Figure 3b and have been calculated as a frequency ratio relative to a frequency spectrum of a random 2 s noise window from each station. The spectral amplitudes of the borehole sensors are all at a similar level, and, therefore, the SNR is also similar at all depths. The highest spectral amplitudes are in the frequency range of 10–100 Hz. This is consistent with all weight drop events. Therefore, all signals recorded by the borehole sensors and the surface array have been filtered between 10 Hz and 100 Hz using a second-order causal Butterworth band pass filter.

The multiple shots of the weight drop have been stacked on the DAS data recorded during VSP-II. This resulted in a significant improvement in the SNR. Figure 4 shows a wavefield of a shot with a distance of 60 m to the well recorded by the fibre optic cable and overlaid by the signals recorded at the borehole sensors (colour-coded traces; cf., Figure 3). The dashed white traces indicate the water wave travelling inside the water-filled borehole with a P-wave of 1480 m/s. The P-wave first arrivals of the DAS section and the borehole sensors at the corresponding depth agree for this example. However, we later present an example where the first arrivals of two exemplary DAS shots are shifted (see, Figure 5a–c) and had to be corrected (Figure 5d–k).

Our input data for the tomography are traveltimes between the shot points and the receivers, which can be calculated from the measured shot times and the P-wave arrival times at the receivers. We manually picked the P-wave arrivals at the seismic sensors, where the onsets are generally impulsive and easy to measure. The DAS data have many more channels that are very similar in their appearance so that a semi-automatic picking approach was used. We manually selected one trace with a clear first onset and cross-correlated the remaining traces in order to estimate the phase shift between the traces, similarly to successive template matching of neighbouring traces (e.g., Gibbons & Ringdal, 2006). This approach worked reliably well and was efficient for DAS. As the borehole chain and the DAS behind the casing were almost co-located, we expected to obtain very comparable arrival times. Figure 5a–c compares the traveltimes of the borehole picks and the

DAS picks for three exemplary weight drop events with different distances to the well (25, 175, 325 m). A systematic average time shift between the borehole sensors and the DAS is observed, which is 0.0195 s for the event with a distance of 25 m and 0.0117 s for the event with a distance of 175 m. The average time shift for the distant weight drop event in 325 m is 0.0008 s. This result indicates that the clock of the DAS interrogator was possibly slightly drifting. Luckily, as both sensor types (borehole sensors and DAS) were almost co-located, we were able to correct the non-static time drift. We calculated an average time shift per weight drop event and corrected the DAS arrival times accordingly (c.f., Figure 5a–c, black dots). The time residuals after the shift correction are smaller than 0.0012 s for all three example events. Figure 5d–k shows a histogram for the time shifts of all drop weight events before (grey bars) and after the time correction (colour-coded bars). Before the time shift correction, the time shift between the borehole sensor picks and the DAS picks ranges between ± 50 samples for all weight drop events. After the shift correction, the time difference has a maximum of ± 20 samples. The mode for all events after the shift correction is ± 4 samples which means a shift of ± 0.004 s at a sampling rate of 1000 Hz.

TOMOGRAPHY

We aim to obtain a local 3D P-wave velocity tomography in order to image structural features. The tomography is based on the first arrivals of P-waves and has been computed using Simulr16 (Bleibinhaus & Gebrande, 2006; Bleibinhaus & Hilberg, 2012), which is based on the approach of Thurber (1983) and Evans et al. (1994). The method, based on the eikonal solver, computes travel-time fields and seismic rays for a given gridded velocity model (Hole & Zelt, 1995). The advantage of the eikonal solver is a high traveltime accuracy for seismic rays and a small computational time for an arbitrary number of receivers. The tomography itself, that is, the inversion for an updated velocity model, is non-linear and is solved incrementally by linear approximations. The method uses a damped least-square inversion to iteratively find a velocity model with small residuals while keeping the changes in the model as small as possible. The model perturbation is controlled by the damping factor, which is estimated beforehand by a damping test. The inversion is repeated iteratively, and the final model is obtained when the parameters (e.g., weighting, damping) are adjusted and, hence, the inversion is stabilized. We first constructed a homogeneous starting model with a P-wave velocity of 3 km/s, chosen from averaged P-wave velocity estimates at different depths. The volume used for the inversion is defined by the array aperture and the borehole depth. Accordingly, the size

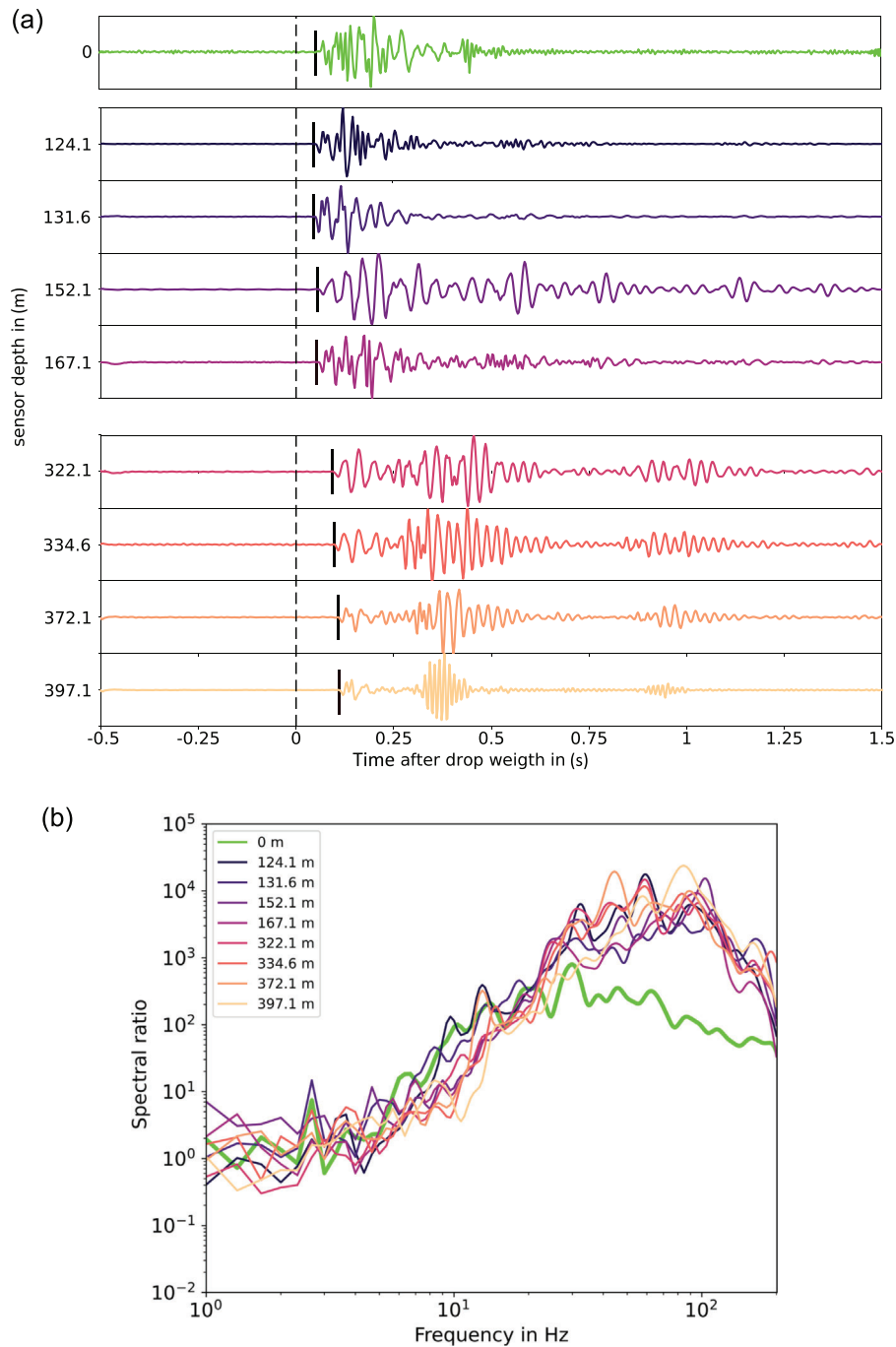


Figure 3 (a) Seismogram section (vertical component) showing one exemplary surface shot (weight drop) with a distance of 58 m to the well. The surface sensor (0 m depth, green) has a distance of 160 m to the well. The borehole sensors are colour-coded with depth. The black dashed line marks the trigger time of the shot at 0 s. The black solid lines show the manually picked first onset of the weight drop induced seismic signals. (b) Corresponding frequency spectra of A. The frequency spectra have been smoothed after Konno and Ohmachi (1998) and are relative to a frequency spectrum of a random seismic noise window of 2 s. The highest amplitudes of the frequency spectrum are in the range of 10–100 Hz. Since the frequency range for the borehole and surface sensors is comparable, we filtered each seismogram in the frequency range of 10–100 Hz.

of the model is $x = 700$ m, $y = 550$ m and $z = 450$ m (Table 2). We used a grid spacing of Δx , Δy , $\Delta z = 5$ m. In a further approach, we refined the initial homogeneous starting model to a two-layered velocity model with low P-velocities overlaying bedrock. This resulted

in a new two-layer starting model consisting of an upper layer with a thickness of 20 m and P-wave velocities of 2.5 km/s followed by a deeper layer with P-wave velocities of 4 km/s (Table 2). The bottom of the model is constrained by the deepest sensors at a depth of 400 m.

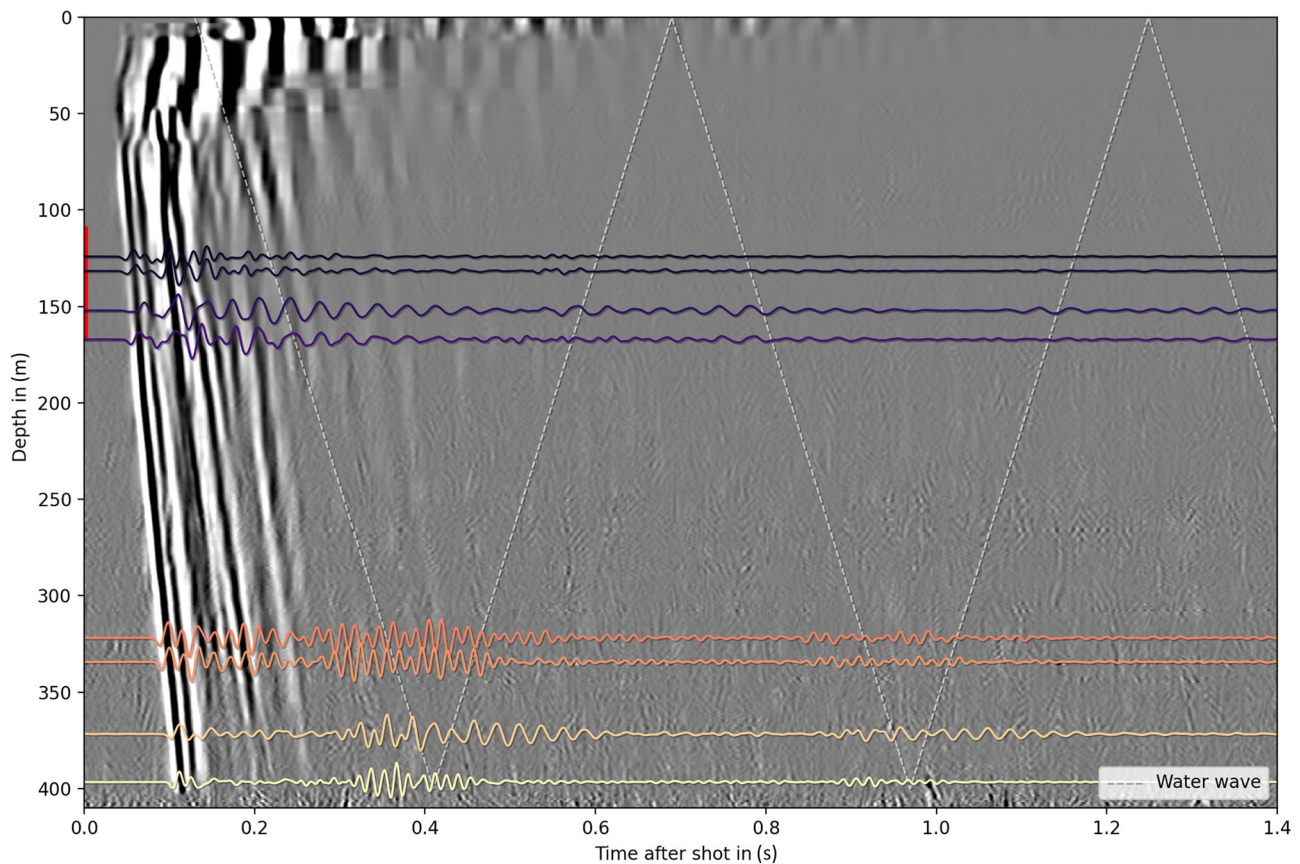


Figure 4 Wavefield of a shot from 60 m distance to the borehole, recorded by DAS on the encased fibre optical cable. Overlaid are the vertical waveforms recorded by the borehole array. The data have been de-noised with the adaptive frequency filter (Isken et al., 2022) (two-passes) and low-pass filtered below 100 Hz. The dashed white line shows the modelled water wave travelling inside the borehole ($v_p = 1480$ m/s). The red vertical line at the x-axis indicates the approximate depth of a diffuse wavefield.

Table 2 Starting models and P-wave velocities in km/s.

Model type	Layer thickness (m)	x-y-z dimension (m)	P-wave velocity (km/s)
Homogeneous	0–450	700×550×450	3
Two layered	0–20	700×550×20	2.5
	20–450	700×550×430	4.0

The 3D ray coverage for both VSP experiments is shown in Figure 6a and is typically used to estimate the confidence of the model which becomes higher when the density of the ray paths crossing a cell in the model increases. Due to the DAS cable and the borehole sensors, the highest ray coverage is in the vicinity of the well. As the seismic rays are also recorded by the surface array, the ray coverage is also high at shallower depths of up to about 50 m. However, the ray coverage becomes poor at the edges and the bottom of the model.

Another approach to estimate the ray coverage is given by the derivative weight sum (DWS; see Figure 6b–f). The DWS is an estimate of the total length

of the seismic rays within a cell. In other words, a high DWS corresponds to a high density of the seismic rays and, therefore, to a high confidence of the velocity tomography. Figure 6b–f shows the DWS for different depths (50–400 m). The DWS at depths of 50 m (Figure 6b) is high in the vicinity of the well at $x = y = 0$ m and at depths below 50–60 m due to the surface sensors. Since the seismic rays are no longer received by the surface array at depths below 50–60 m, the DWS and hence the ray coverage is only high in the vicinity of the well at greater depths (Figure 6c). This is also visible at higher depths (e.g., 200 m) where the area of the DWS becomes smaller with a peak at the position close

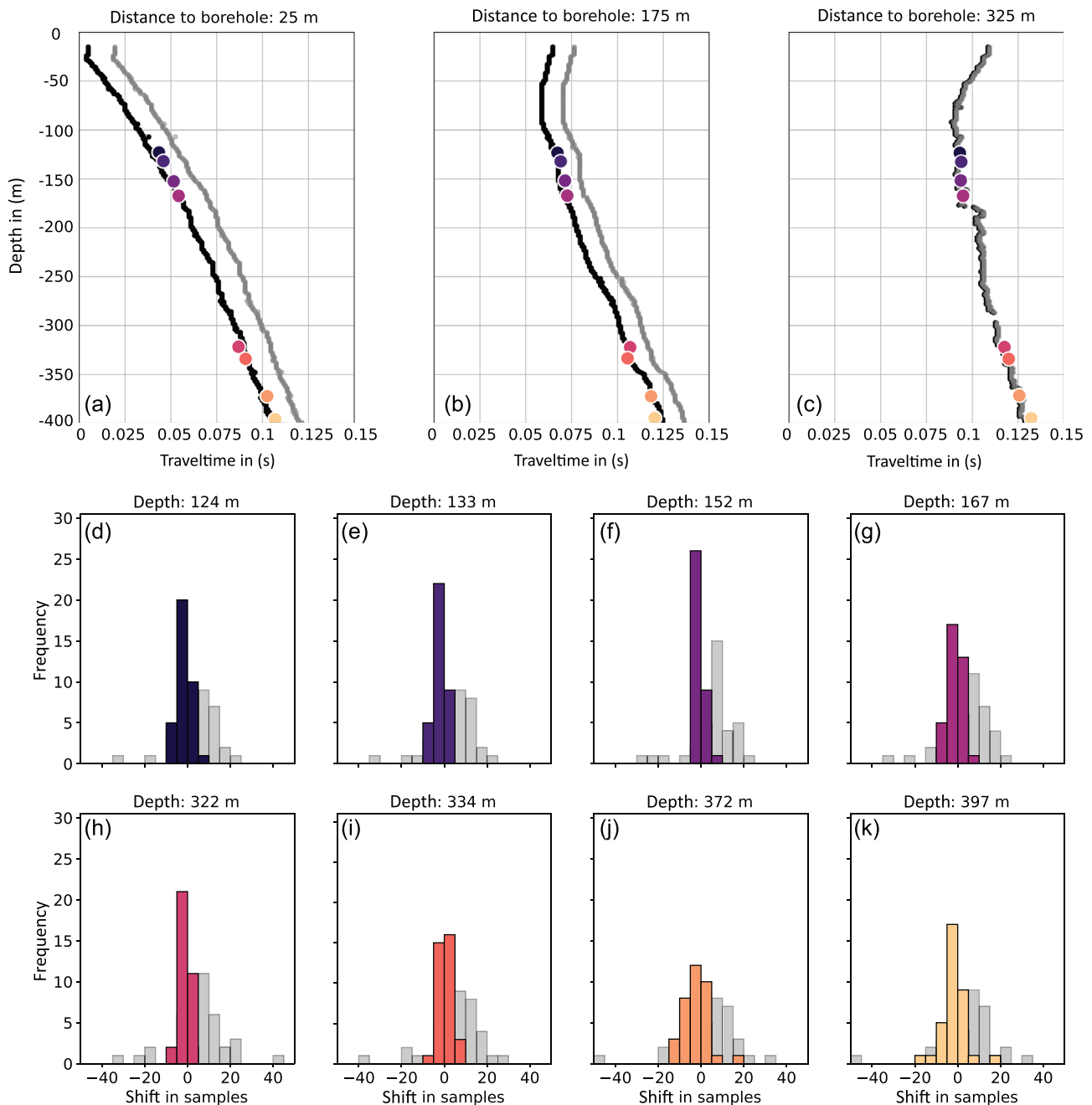


Figure 5 (a)–(c) Traveltime versus depth between the borehole sensor traveltimes (colour-coded dots) and the DAS traveltimes for three exemplary weight drop events with a distance of 25 m (a), 175 m (b) and 325 m (c) to the well. The black dots show the corrected DAS times after the time shift correction. (d)–(k) Histogram showing the time shift between the DAS picks after the time shift correction and the borehole picks (colour coded). The time shift before the correction is shown in grey. The average time shift after the shift correction is less than ± 0.01 s for all weight drop events. The mode for each sensor depth and shot event is less than ± 0.004 s.

to the well at $x = y = 0$ m (cf., Figure 6d,e). At 400 m depth, the seismic rays are only received by the borehole sensors and the DAS cable, resulting in a low ray coverage towards the bottom of the model (Figure 6f).

The final 3D P-wave velocity tomography is shown in Figures 7 and 8. As our goal is to image a steep,

shallow fault zone, we show a cross section of the 3D tomography along a SW-NE profile, which is oriented perpendicular to the strike of the assumed fault zone (Figure 1b, black dashed line after Saxon State Office for Environment, Agriculture and Geology, 2022). Figure 8a–h shows several horizontal sections at

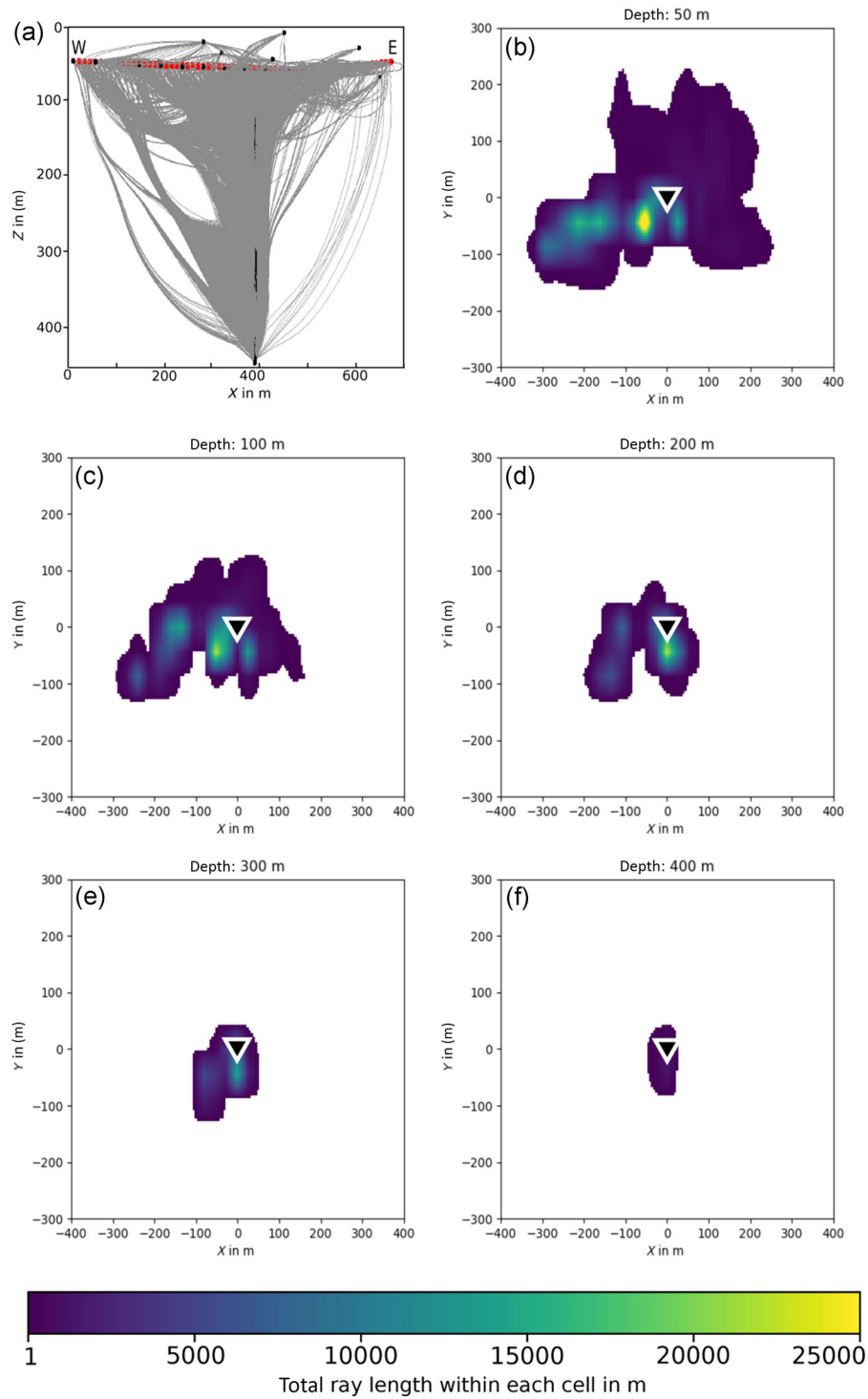


Figure 6 (a) Model showing the seismic rays of the weight drop induced seismic signals. The black squares represent the receiver of both VSP experiments (surface arrays, borehole geophones and DAS cable). The red squares show the position of the weight drop events. The seismic rays are shown in grey. (b)–(f) Derivative weight sum showing the total ray length within each cell as a measure of the ray coverage in different depths (50–400 m). The white edged triangles show the position of the well. The derivative weight sum is high, close to the surface due to the surface array and close to the well due to the high resolution of the DAS cable.

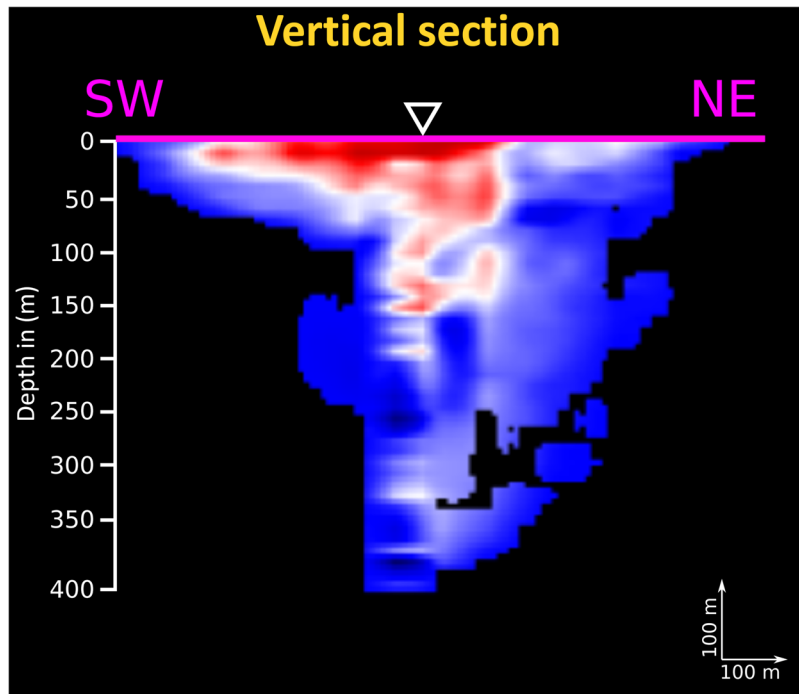


Figure 7 Vertical section of the 3D velocity tomography in the x - and z -directions of the SW-NE profile (cf. Figure 1) which is normal to the postulated fault zone here shown as a magenta line. The horizontal slices (x - and y -directions) of the 3D velocity tomography at different depths are shown in Figure 8.

different depths. The tomography only considered cells with a DWS greater than 1. In other words, the P-wave velocities are only shown if a cell consists of at least 1 m of seismic rays (the traveltime of a seismic ray in a 1-m segment at the surface is about 0.001 s).

The vertical section shows a SW-NE profile of the 3D tomography (cf., Figure 1, black line) with a high contrast of the P-wave velocities close to the surface and at higher depths in the vicinity of the well (Figure 7). There is a horizontal low-velocity zone (LVZ, red area) with P-wave velocities between 1000 m/s and 3000 m/s up to depths of about 30–50 m. At greater depths, the horizontal LVZ decreases but is still visible close to the borehole at depths of up to about 160 m with P-wave velocities up to 3000 m/s (Figure 7). The higher P-wave velocities outside the LVZ (blue area) are between 3000 m/s and 5000 m/s and increase with depth.

Figure 8a–h shows horizontal slices of the P-wave velocity tomography at several depths (0, 15, 30, 50, 90, 120, 165 and 350 m). The P-wave velocities at the surface (0 m) show a sharp transition between the lower P-wave velocities (1500–3000 m/s; red area) and the higher P-wave velocities (up to 4000 m/s). The LVZ at the surface has a size of 300 m in the x -direction and 200 m in the y -direction (Figure 8a, red area). The LVZ and, hence, the high contrast of the P-wave velocities decreases at depths of 30 m (Figure 8b,c). Up to depths of 120 m, the high contrast of the P-wave velocities is only visible close to the borehole indicating that the LVZ crosses the borehole at these depths (Figure 8d–f). The inverted P-wave velocities outside the LVZ range from 3000 to 5000 m/s. However, the P-wave velocity does

not change significantly at greater depths and is about 4000–5000 m/s (Figure 8g,h).

DISCUSSION

The main objective of the VSP experiments was a local 3D seismic velocity tomography of the uppermost 400 m within the study area including the characterization of a steep, non-tectonic fault zone that was first recognized during drilling. The 3D velocity tomography (Figures 7 and 8) indicates P-wave velocities between 1500 m/s and 5000 m/s within a shallow, horizontal (up to 50 m) LVZ with P-wave velocities between 1000 m/s and 3000 m/s (red area, Figure 8) and higher P-wave velocities in greater depths of up to 5000 m/s (blue area). In addition, the LVZ also occurs at greater depths of up to 165 m (Figure 7, red area) and crosses the borehole at a depth between 90 m and 165 m with a dip of approximately 60°. We identified the LVZ based on a strong P-wave velocity contrast at this depth. Figure 8a–h shows several horizontal slices of the 3D velocity tomography at different depths (0, 15, 30, 50, 90, 120, 165 and 350 m). The horizontal slices show an apparent decrease in the width of the LVZ with depth. While the LVZ (red area) has a size of about 500×250 m in the x – y direction at the surface (Figure 8a), the size of the LVZ decreases at depths of 15 m and 30 m (Figure 8b,c). However, the size of the LVZ at the surface coincides with the array aperture of the two VSP experiments. The ray coverage and hence the confidence at the edge of the model is poor which may explain the size of the LVZ and the high contrast to

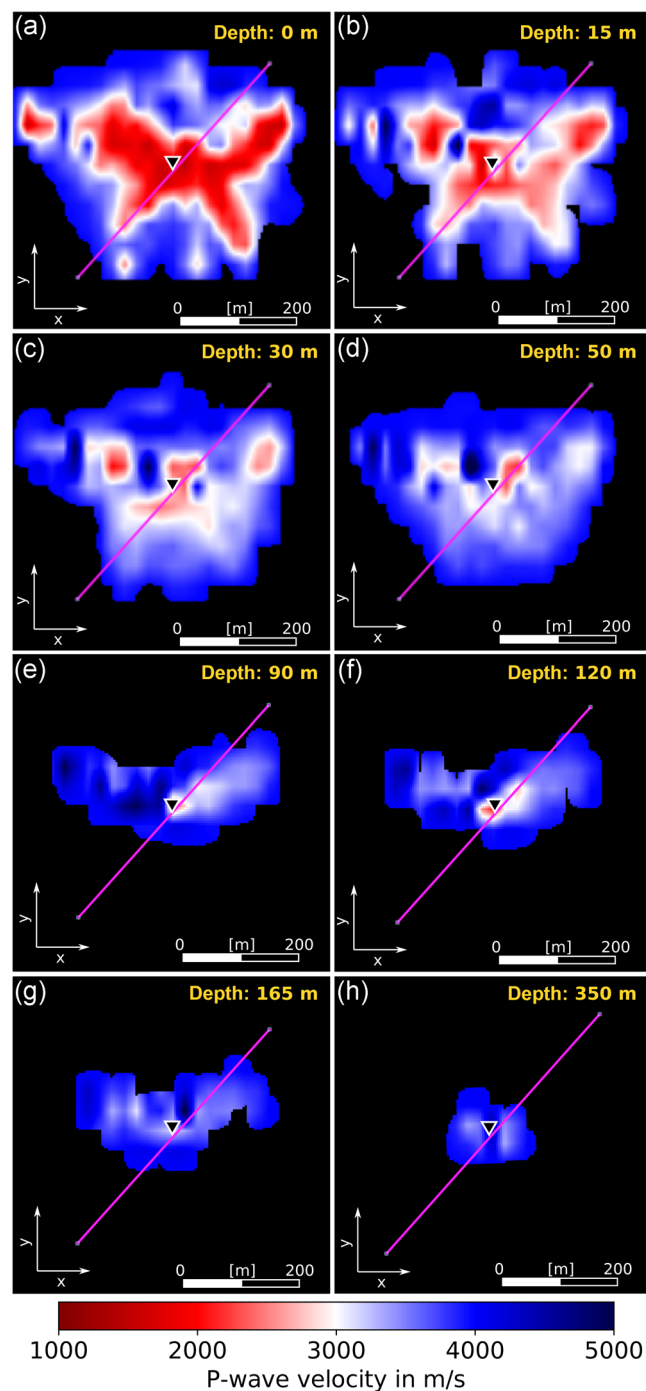


Figure 8 (a)–(h) Horizontal slices (x - and y -directions) of the 3D velocity tomography at different depths. The white edged black triangle shows the position of the well. The magenta line is the SW-NE profile normal to the fault zone corresponding to the vertical section of Figure 7.

the higher P-wave velocities at the edge at the surface. However, the LVZ is still visible at a depth of 50 m (Figure 8d). For greater depths, the LVZ is only visible close to the borehole, suggesting that the LVZ is only present close to the borehole (white edged black triangle, Figure 8e,f). However, this could also be due to ray coverage and our array instrumentation. Based

on the 3D velocity tomography, we identified an LVZ with P-wave velocities of up to 3000 m/s in the shallow subsurface and crossing the borehole at a depth of 90–165 m with a dip of about 60°. At greater depths, the LVZ moves away from the well and cannot be resolved anymore. The P-wave velocities increase gradually with depth up to 5000 m/s (cf., Figure 7).

The logging data (Figure 2) obtained during the drill also provide information about the LVZ and the associated fault zone. Figure 2a shows the core recovery with depth. The core recovery is poor near the surface (up to a depth of 30 m) and at greater depths between 90 m and 165 m (marked with red lines) and 365–390 m. The shallow poor core recovery can be explained by soil and weathered material (mainly silty-sandy matrix and sand-silty phyllite) and coincides with the depth of the shallow horizontal LVZ (cf., Figure 1c). The deeper poor core recovery up to a depth of 165 m cannot be influenced by weathering processes but indicates an intensely fractured material or a fault zone (Figure 2a). This is also the depth where the drill mud was lost. In addition, Figure 2b shows the EC. At a depth between 90 m and 165 m (Figure 2b, red lines), where we expect the fault zone, the median EC is 0.0075 mS/m (maximum EC of 0.0182 mS/m). The median EC beyond the depth of the fault zone is 0.0018 mS/m, and the EC within the fault zone is four times higher than the median EC beyond the fault zone. High EC occurs when a medium is corrosive. For example, corrosive material is formed when water enters cracks with high porosity and thus dissolves the rock through chemical changes. Fractured material, cracks and chemical changes are also evidence of a fault zone. Based on the logging data, we interpret the deeper LVZ (depth: 90–165 m) as a fault zone crossing the borehole at a depth of 90–165 m.

An interesting question for further study is whether fault zones can be identified and characterized by wavefields using only a portable fibre optic cable in an existing well. Figure 6 shows the DAS wavefield recorded by the fibre optic cable. The traveltimes of the waveforms recorded at the uppermost 20 m are slightly delayed compared to the waveforms recorded at greater depths. This can be explained by the lower P-wave velocities of the shallow horizontal LVZ (soil and weathering material; cf., Figures 7 and 1c). At a depth of about 90–165 m (Figure 6, red vertical line), the wavefield is diffuse, especially the first arrivals are indistinct and the waveforms have experienced more attenuation. The diffuse waveforms are recorded within the depth of the expected fault zone (90–165 m; see, Figures 1c, 2a and 7). The waveforms in greater depths have again clear first arrivals. As the vertical spacing between the fibre channels is 1 m, the DAS wavefield allows high-resolution imaging of subsurface structures with depths. Thus, imaging the subsurface using DAS waveforms provides an initial detection of a possible fault zone. A temporary fibre optic cable can be brought into an existing borehole for an initial detection of a shallow fault zone. For example,

the fibre optic cable in combination with a weight drop (in our case an SDD 6600 drop weight) can be used as a simple tool for the initial characterization of shallow fault zones.

The experiments revealed difficulties and sources of error in the integration of borehole data with DAS data. For example, the SNRs were low for the shots recorded by DAS. We, therefore, repeated the shots three times at the source position of the VSP-II in order to stack the data, which resulted in a significant increase in the DAS SNRs. The first arrivals recorded by DAS and the borehole sensors match for some shots (see Figure 4), but we identified a non-static time shift in the DAS data for several shots (cf., Figure 5). We interpret the time shift as a drifting clock issue of the DAS interrogator. As the borehole sensors and the DAS cable are co-located in the borehole, we rule out an earlier arrival of the P-waves at DAS. After correcting the time shift by subtracting an average time shift from the DAS traveltimes per shot, we were able to reduce all time shifts to less than ± 0.02 s with a median time shift of 0.004 s.

As steep fault zones are suitable reservoir targets and thus of high interest for geothermal studies, our VSP experiments provide an example to image fault zones using active experiments. Figure 6a shows the ray coverage for both VSP experiments and several horizontal sections showing the DWS with depth. The ray coverage is typically used to find the highest confidence of the seismic tomography. As the ray coverage is low at the edge of our study area, we only consider grid cells with a minimum ray length of 1 m. This results in a V-shape of the 3D tomography (Figure 7). In our experiments, we had the advantage of a 400-m deep borehole instrumented with borehole geophones and a fibre optic cable. In order to find suitable geothermal reservoirs, the question arises whether to image fault zones using only a temporary surface array. However, the ray coverage of the uppermost 50 m is high due to the distribution of the surface sensors but gets less with larger depth (Figure 6b–f). In addition, the ray coverage and the DWS are high down to 400 m close to the borehole due to the borehole sensors and especially due to the high-resolution fibre optic cable. In our experiments, the surface arrays only record seismic rays down to a depth of about 50 m (cf., Figure 6) and, hence, we were not able to image the fault zone down to a depth of 165 m using only a surface array. However, to get the first indication of a fault zone, it would be possible to install a temporary fibre optic cable within an existing borehole which is close to a fault zone.

CONCLUSION

In conclusion, as shallow steep non-tectonic fault zones are suitable for geothermal reservoirs, our VSP exper-

iments present a simple strategy for characterizing such fault zones. The maximum resolved depth of the study area is limited by the type of the seismic source (here: weight drop, 340 kg, SDD 6600) and by the lowest sensors in the borehole (400 m). In our case, a temporary surface array only would not be able to image fault zones. However, the high-resolution wavefield recorded by the fibre optic cable can be used for the initial detection and characterization of such fault zones. According to that, VSP experiments combined with a portable weight drop and a temporary fibre optic cable within an existing borehole provide a useful tool for geothermal studies in order to identify near-surface, steep fault zones as potential geothermal reservoirs.

ACKNOWLEDGEMENTS

The research is funded by the Deutsche Forschungsgemeinschaft (DFG, German Research Foundation) under the project numbers 419909358 and 419455546. We thank the Saxon State Office for Environment, Agriculture and Geology, which finances the surface array used in the second VSP experiment. The seismological instruments were kindly provided by the Geophysical Instrument Pool Potsdam (GIPP) at GFZ Potsdam. We also thank Theresa Rein, Juliane Starke and Jonas Pätzelt for technical support in the field.

CONFLICT OF INTEREST STATEMENT


The authors have declared no conflict of interest and agree on this publication.

DATA AVAILABILITY STATEMENT

The data used in this study are available upon request to the corresponding authors and will be made available at the GEOFON Data Archive.

ORCID

Nikolaus Rein  <https://orcid.org/0009-0002-5165-0946>

Katrin Hannemann  <https://orcid.org/0000-0003-3782-1606>

REFERENCES

- Babuška, V., Plomerová, J. & Fischer, T. (2007) Intraplate seismicity in the Western Bohemian massif (central Europe): a possible correlation with a paleoplate junction. *Journal of Geodynamics*, 44(3–5), 149–159.
- Balch, A.H. & Lee, M.W. (1984) *Vertical seismic profiling: technique, applications, and case histories*. Boston, MA: International Human Resources Development Corporation.
- Bankwitz, P., Schneider, G., Kämpf, H. & Bankwitz, E. (2003) Structural characteristics of epicentral areas in Central Europe: study case Cheb Basin (Czech Republic). *Journal of Geodynamics*, 35(1–2), 5–32.
- Bleibinhaus, F. & Gebrande, H. (2006) Crustal structure of the Eastern Alps along the Transalp profile from wide-angle seismic tomography. *Tectonophysics*, 414(1–4), 51–69.
- Bleibinhaus, F. & Hilberg, S. (2012) Shape and structure of the Salzach Valley, Austria, from seismic traveltime tomography and

- full waveform inversion. *Geophysical Journal International*, 189(3), 1701–1716.
- Bräuer, K., Kämpf, H. & Strauch, G. (2009) Earthquake swarms in non-volcanic regions: What fluids have to say. *Geophysical Research Letters*, 36(17), L17309.
- Bräuer, K., Kämpf, H., Strauch, G. & Weise, S.M. (2003) Isotopic evidence ($^3\text{He}/^4\text{He}$, $^{13}\text{C}_{\text{CO}_2}$) of fluid-triggered intraplate seismicity. *Journal of Geophysical Research: Solid Earth*, 108(B2), 2070.
- Cai, J., McMechan, G.A. & Fisher, M.A. (1996) Application of ground-penetrating radar to investigation of near-surface fault properties in the San Francisco Bay region. *Bulletin of the Seismological Society of America*, 86(5), 1459–1470.
- Chen, T. & Huang, L. (2015) Directly imaging steeply-dipping fault zones in geothermal fields with multicomponent seismic data. *Geothermics*, 57, 238–245.
- Corbel, S., Schilling, O., Horowitz, F., Reid, L., Sheldon, H., Timms, N. & Wilkes, P. (2012) Identification and geothermal influence of faults in the Perth Metropolitan Area, Australia. Paper presented at the Thirty-seventh workshop on geothermal reservoir engineering, Stanford, CA.
- Credner, H. (1898) ... Die sächsischen erdbeben während der jahre 1889 bis 1897: insbesondere das sächsisch-böhmisch erdbeben vom 24. oktober bis 29. november 1897, volume 24. BG Teubner.
- Dahm, T., Fischer, T. & Hainzl, S. (2008) Mechanical intrusion models and their constraints on the density of fluids injected in the NW Bohemia Swarm region at 10 km depth. *Studia Geofísica*, 52, 529–548.
- Dahm, T., Horálek, J. & Šílený, J. (2000) Comparison of absolute and relative moment tensor solutions for the January 1997 West Bohemia earthquake swarm. *Studia Geophysica et Geodaetica*, 44(2), 233–250.
- Dahm, T., Hrubcová, P., Fischer, T., Horálek, J., Korn, M., Buske, S., & Wagner, D. (2013) Eger rift ICDP: an observatory for study of non-volcanic, mid-crustal earthquake swarms and accompanying phenomena. *Scientific Drilling*, 16, 93–99.
- Demanet, D., Renardy, F., Vanneste, K., Jongmans, D., Camelbeek, T. & Meghraoui, M. (2001) The use of geophysical prospecting for imaging active faults in the Roer Graben, Belgium. *Geophysics*, 66(1), 78–89.
- Evans, J.R., Eberhart-Phillips, D. & Thurber, C. (1994) User's manual for SIMULPS12 for imaging V_p and V_p/V_s ; a derivative of the "Thurber" tomographic inversion SIMUL3 for local earthquakes and explosions. Technical report. Denver, CO: US Geological Survey.
- Fischer, T., Horálek, J., Hrubcová, P., Vavryčuk, V., Bräuer, K. & Kämpf, H. (2014) Intra-continental earthquake swarms in West-Bohemia and Vogtland: a review. *Tectonophysics*, 611, 1–27.
- Fischer, T., Hrubcová, P., Dahm, T., Woith, H., Vylita, T., Ohrnberger, M., Vlček, J., Horálek, J., Dědeček, P., Zimmer, M., et al. (2022) ICDP drilling of the Eger Rift Observatory: magmatic fluids driving the earthquake swarms and deep biosphere. *Scientific Drilling*, 31, 31–49.
- Fischer, T. & Michálek, J. (2008) Post 2000-swarm microearthquake activity in the principal focal zone of West Bohemia/Vogtland: space-time distribution and waveform similarity analysis. *Studia geophysica et geodaetica*, 52(4), 493–512.
- Gibbons, S.J. & Ringdal, F. (2006) The detection of low magnitude seismic events using array-based waveform correlation. *Geophysical Journal International*, 165(1), 149–166.
- Goyal, K. & Kassoy, D. (1980) Fault zone controlled charging of a liquid-dominated geothermal reservoir. *Journal of Geophysical Research: Solid Earth*, 85(B4), 1867–1875.
- Hainzl, S. & Fischer, T. (2002) Indications for a successively triggered rupture growth underlying the 2000 earthquake swarm in Vogtland/NW Bohemia. *Journal of Geophysical Research: Solid Earth*, 107(B12), ESE-5.
- Hainzl, S., Fischer, T. & Dahm, T. (2012) Seismicity-based estimation of the driving fluid pressure in the case of swarm activity in Western Bohemia. *Geophysical Journal International*, 191(1), 271–281.
- Haldar, S.K. (2020) *Introduction to mineralogy and petrology*. Amsterdam: Elsevier.
- Hergesell, W. (2022) *Mineralogisch-strukturelle Untersuchungen an Bohrkernen der Landwüst-Bohrung, Vogtland*. Potsdam: Universität Potsdam.
- Hole, J. & Zelt, B. (1995) 3-D finite-difference reflection traveltimes. *Geophysical Journal International*, 121(2), 427–434.
- Horálek, J. & Fischer, T. (2008) Role of crustal fluids in triggering the West Bohemia/Vogtland earthquake swarms: just what we know (a review). *Studia Geophysica et Geodaetica*, 52(4), 455.
- Horálek, J. & Fischer, T. (2010) Intraplate earthquake swarms in West Bohemia/Vogtland (Central Europe). *Jökull*, 60, 67–87.
- Hrubcová, P., Geissler, W.H., Bräuer, K., Vavryčuk, V., Tomek, Č. & Kämpf, H. (2017) Active magmatic underplating in western Eger Rift, Central Europe. *Tectonics*, 36(12), 2846–2862.
- Hrubcová, P., Vavryčuk, V., Boušková, A. & Horálek, J. (2013) Moho depth determination from waveforms of microearthquakes in the West Bohemia/Vogtland swarm area. *Journal of Geophysical Research: Solid Earth*, 118(1), 120–137.
- Improta, L. & Bruno, P. (2007) Combining seismic reflection with multi-fold wide-aperture profiling: an effective strategy for high-resolution shallow imaging of active faults. *Geophysical Research Letters*, 34(20), L20310.
- Isken, M.P., Vasyura-Bathke, H., Dahm, T. & Heimann, S. (2022) De-noising distributed acoustic sensing data using an adaptive frequency-wavenumber filter. *Geophysical Journal International*, 231(2), 944–949.
- Ivanov, J., Miller, R.D., Lacombe, P., Johnson, C.D. & Lane, J.W., Jr, (2006) Delineating a shallow fault zone and dipping bedrock strata using multichannel analysis of surface waves with a land streamer. *Geophysics*, 71(5), A39–A42.
- Konno, K. & Ohmachi, T. (1998) Ground-motion characteristics estimated from spectral ratio between horizontal and vertical components of microtremor. *Bulletin of the Seismological Society of America*, 88(1), 228–241.
- Lellouch, A., Yuan, S., Spica, Z., Biondi, B. & Ellsworth, W. (2019) Seismic velocity estimation using passive downhole distributed acoustic sensing records: examples from the San Andreas Fault Observatory at depth. *Journal of Geophysical Research: Solid Earth*, 124(7), 6931–6948.
- Lutter, W.J., Fuis, G.S., Thurber, C.H. & Murphy, J. (1999) Tomographic images of the upper crust from the Los Angeles Basin to the Mojave Desert, California: results from the Los Angeles Region seismic experiment. *Journal of Geophysical Research: Solid Earth*, 104(B11), 25543–25565.
- Miller, R.D., Steeples, D.W. & Brannan, M. (1989) Mapping a bedrock surface under dry alluvium with shallow seismic reflections. *Geophysics*, 54(12), 1528–1534.
- Nizkous, I., Gerritsen, S., Kiyashchenko, D. & Joinson, D. (2015) Distributed acoustic sensing (DAS) VSP for imaging and velocity model building. Paper presented at the International Petroleum Technology Conference. Doha, Qatar, December 2015. OnePetro.
- Othonos, A. (2000) Bragg gratings in optical fibers: fundamentals and applications. In: Grattan, K.T.V. & Meggiiti, B.T. (Eds) *Optical fiber sensor technology*. Boston, MA: Springer, pp. 79–187.
- Özbek, A., Gül, M., Karacan, E. & Alca, Ö. (2018) Anisotropy effect on strengths of metamorphic rocks. *Journal of Rock Mechanics and Geotechnical Engineering*, 10(1), 164–175.
- Saxon State Office for Environment, Agriculture and Geology. (2022) Geology and fault zones of Saxony. <https://geoviewer.sachsen.de/mapviewer2/index.html?lang>.
- Stephenson, W., Smith, R. & Pelton, J. (1993) A high-resolution seismic reflection and gravity survey of quaternary deformation across the

- Wasatch Fault, Utah. *Journal of Geophysical Research: Solid Earth*, 98(B5), 8211–8223.
- Thurber, C.H. (1983) Earthquake locations and three-dimensional crustal structure in the Coyote Lake Area, Central California. *Journal of Geophysical Research: Solid Earth*, 88(B10), 8226–8236.
- Vavryčuk, V. (2011) Principal earthquakes: theory and observations from the 2008 West Bohemia swarm. *Earth and Planetary Science Letters*, 305(3–4), 290–296.
- Vavryčuk, V., Bouchaala, F. & Fischer, T. (2013) High-resolution fault image from accurate locations and focal mechanisms of the 2008 swarm earthquakes in West Bohemia, Czech Republic. *Tectonophysics*, 590, 189–195.

How to cite this article: Rein, N., Isken, M.P., Domigall, D., Ohrnberger, M., Hannemann, K., Krüger, F., Korn, M., et al. Dahm, T. (2024) Characterizing shallow fault zones by integrating profile, borehole and array measurements of seismic data and distributed acoustic sensing. *Near Surface Geophysics*, 22, 298–312. <https://doi.org/10.1002/nsg.12293>